Original Article

Effects of sintering temperature on the microstructure, mechanical, tribological and thermophysical properties of GNPs/IN738 composite

Olugbenga Ogunbiyi [a,*], Tamba Jamiru [a], Rotimi Sadiku [b], Smith Salifu [c], Charity Maepa [d]

[a] Department of Mechanical and Mechatronics Engineering, Tshwane University of Technology, Pretoria 0001, South Africa
[b] Department of Chemical, Metallurgical and Materials Engineering, Tshwane University of Technology, Pretoria 0001, South Africa
[c] Centre for NanoMechanics and Tribocorrosion, School of Mining, Metallurgy and Chemical Engineering, University of Johannesburg, South Africa
[d] Department of Physic, Laboratory for Microscopy and Microanalysis, University of Pretoria, Hartfield 0028, Pretoria, South Africa

ARTICLE INFO

ABSTRACT

While IN738 Ni-based superalloy is a high strength alloy, it is feasible to improve its properties at the bulk level by reinforcing with graphene nanoplatelets (GNPs), taking advantage of the superior mechanical, tribological and thermal properties using the spark plasma sintering technique. In the present study, the influence of spark plasma sintering temperature range between 900 and 1100 °C on the microstructure, mechanical, tribological and thermophysical properties of GNPs/IN738 composite is assessed. The dispersion of GNPs reinforcement and alloying metals to form composite powder is conducted using a turbular mixer and low-frequency planetary ball milling, followed by spark plasma sintering. The relative density of the sintered samples assessed following Archimedes' method indicates increasing densification with the increasing sintering temperature from 94.7% (900 °C) to 98.5% (1100 °C). The microstructure assessed via SEM, XRD and Raman spectroscopy indicates the formation of precipitate gamma, intermetallic gamma prime, solid solution and GNPs strengthening phases. Thus, the mechanical (micro/nano hardness and Young's modulus), tribological (wear rate and coefficient of friction), and thermophysical (thermal diffusivity, thermal conductivity, and specific heat capacity) properties increased with the increasing sintering temperature. The microhardness increased from 354HV (900 °C) to 469HV (1100 °C), nanohardness from 8 GPa (900 °C) to 17 GPa (900 °C), and Young's modulus from 190 GPa (900 °C) to 291 GPa (1100 °C). The wear rate reduced with an increase in sintering temperature for the three loads of 5, 10 and 20N. The thermophysical properties assessed from 25 to 600 °C show the formation of few inflection points as the

---

* Corresponding author.
  E-mail address: olugbengaogunbiyi@gmail.com (O. Ogunbiyi).

temperature increases, which is attributed to the dissolution and rearrangement of precipitate gamma prime and Cr in solid solution phases. Similarly, the small increment in the thermal diffusivity is equally associated with the smoother phonon transition at the GNPs/matrix interface.

1.   Introduction

Ni-based superalloys are an exceptional group of metallic materials widely used for different engineering applications. They show an extraordinary combination of properties such as high-temperature strength, toughness and resistance to oxidation/corrosion attack [1]. Other properties include good structural stability, resistance to fatigue and high elastic modulus. Owing to these properties, they are classified as an essential material, especially in the aerospace, power generation, oil and gas, chemical and automobile industries [2]. The alloys are used to fabricate components of the turbine system in aircraft and power plant engines, drillers in oil and gas, and engine parts in nuclear power and chemical processing plants. Several Ni-based superalloys exist, such as Inconel, Hastaloy, Waspaloy, Nimonic, Udimet, Rene', CMSX and Mar [3]. One of the groups that have found broader applications in the industries is the Inconel group, and Inconel 738 has successfully been applied for fabricating various engineering components [4]. Ni element served as the matrix material, usually in the range of 40−65% of the total composition [5]. The alloys possess good mechanical and material properties that enable them to function at a temperature close to their melting temperature (90% of the melting temperature). This is attributed to the face-centred cubic (FCC) structural formation, aided by the presence of precipitate intermetallic phase, hard solid solution phase and carbide phase [6].

The alloys are designed to gain strength from the solid solution strengthening process brought about by adding refractory metal elements such as W, Mo, Ta and Cr. Aside from the phases mentioned, the strength is further improved by the contribution of the precipitate matrix and intermetallic phases (γ-matrix, γ' and γ''). The gamma matrix phase (γ) results from the contribution of Ni matrix element, while the intermetallic gamma prime (γ') and gamma prime prime phase (γ'') results from the reaction of Ti, Al and Nb with the matrix phase ($Ni_3(Ti, Al, Nb)$) [7]. Other elements are added in small quantities to control the mechanical properties and grain structure with the addition of boron and carbon, resulting in the formation of boride and carbide structures. The formation of MC (M = metal atom) carbide results from the strong affinity of carbon to elements such as Hf, Ta, Ti, W, Mo, V, Cr, and Zr [8]. Despite the many advantages of the IN738 Ni-based superalloy, limitations from plastic anisotropy still exist [9]. Therefore, efforts are ongoing to address the improvement of its mechanical properties. This brings about superalloy reinforcement using non-metallic materials for the development of metal matrix composites (MMC). The addition of allotropes of carbon and rare earth elements (metals) have been in use for texture modification of alloys [10], with a careful selection of processing techniques, including heat treatment, especially when an improvement in the mechanical properties of materials is the target.

Graphene is identified as a promising material of choice for reinforcing metals and their alloys [11]. It exists as sheets of sp^2-bonded carbon atoms closely packed in a honeycomb crystal lattice and is relatively recent in the materials science field (2004) [12]. Graphene possesses promising materials and mechanical properties such as excellent thermal conductivity strength (5 kW/m.K), high specific surface area (2630 m^2/g), high strength (125 GPa), high fracture toughness (4.0 ± 0.6 MPa$\sqrt{m}$ in terms of critical stress intensity factor and 15.9 Jm^{-2} in term of the equivalent critical strain energy release rate), charge carrier mobility (2×10^5 cm^2/(V.s)) and high elastic modulus. Graphene incorporation is considered to be an effective and ideal means of optimizing microstructure, improving the microhardness and wear behaviour of a Ni-based superalloy [13,14]. Several unique properties of graphene are documented in the literature, and researchers have been exploring its superior qualities in developing and manufacturing metal matrix composites using different powder metallurgy (PM) methods [15].

One of the methods used is the spark plasma sintering (SPS) technique. SPS is a PM technique that combines the simultaneous application of high current (electric current passing through the powder), high temperature and high pressure through the axial force in densifying powder material into a solid form [16]. The advantages of SPS include rapid densification (between 5 and 40 min), minimal human interference, computer-aided control, and reduction of contamination/impurities during material processing [17]. It uses an ON-OFF direct current (DC) pulse electric current coupled with the application of axial force from the axially positioned piston for powder densification in a one-step operation.

The application of high temperature facilitates the generation of a rapid heating rate at the powder particles' contact points which causes surface melting of particles and upwardly progress to the core of the particle, aiding diffusing and fast sintering. In the process, the materials microstructure is refined, and properties are improved [18]. However, selecting processing parameters can be daunting, especially when the processing parameters can result in different material properties in the sintered product. Such parameters include the heat temperature, pressure, heating rate and soaking time. Although, it has been reported that the heating temperature and pressure are the two most significant paraments in the control of density and mechanical properties of sintered alloys [19−21]. Meanwhile, the fabrication of materials with

high structural integrity is a compelling task for engineers. A good material should have qualities such as good densification, reduced porosity, reduced micro and macro segregation, homogenous phase distribution, reduced structural defects and good mechanical properties, as these affect the service life of a material.

Rominiyi et al. [22] employed the SPS technique in synthesizing and consolidating Ti–2Ni and Ti–10Ni, varying the sintering temperature from 850 to 1200 °C. They reported that the sintered samples' relative density and microhardness reach the maximum at the highest sintering temperature of 1200 °C. Thus, a high sintering temperature promotes good densification and improved mechanical properties. The effect of sintering temperature and pressure on the structural integrity, electrochemical and mechanical properties of Ti–30Ta alloys for biomedical applications was studied by Bayode et al. [23]. Among the combination of sintering temperature, time and pressure of 1200 °C/5 min/30 MPa, 1200 °C/5 min/40 MPa, 1100 °C/10 min/30 MPa and 1100 °C/10 min/ 40 MPa used, sintering pressure has a pronounced contribution in achieving high densification. The combination of 1200 °C/5 min/40 MPa and 1100 °C/10 min/40 MPa resulted in high densification of 98.19% and 98.63%, respectively. Similarly, the sintering performance and alloying effect on commercially pure titanium using sintering temperatures of 800, 1000, and 1100 °C was investigated via the SPS method by Jeje et al. [24]. It was demonstrated that the sintering temperature of 1000 °C promotes good densification and mechanical properties. The factors contributing to the improvement are attributed to the phases formed within the microstructure. In contrast, the samples sintered at 1100 °C display poor densification due to the formation of structural defects.

Furthermore, few other researchers have investigated the influence of SPS sintering temperature in manufacturing metal matrix alloys and composites [21,25–27]. This implies that it plays a vital role in the evolution of the microstructure, densification and improvement of mechanical, tribological, thermophysical and electrochemical properties of the sintered components. Essentially, the existing materials prepared by SPS mainly focus on Ti, Ni alloys and ceramics. Thus, it is imperative to investigate the effect of sintering temperature on the graphene nanoplatelet reinforced Ni-based composites (GNPs/IN738 composite) produced via the SPS method. In this study, the parent material is IN738 superalloy, and the reinforcement is graphene nanoplatelets. The investigation focuses on the resulting relative density, mechanical, tribological and thermophysical properties.

2. Experimental detail

2.1. Materials

The elemental powders that make-up IN738 Ni-based superalloy are sourced from 3 suppliers. These are Ni powder with particle size $\leq$ 44 μm (parent element, 99.5% purity) and Al powder with a particle size of 25 μm (99.8% purity) from TLS-Technik Gmbh, Germany. Ta, W and Ti powder particle size $\leq$ 44 μm (99.5%, 99.8%, 99.8% purity) from Sigma Aldrich, South Africa. Co and Cr have a particle size of $\leq$ 44 μm (99.9%)

provided by Alfa Aesar, South Africa. Sigma Aldrich supplies the graphene nanoparticles (GNPs) reinforcement with product code 900,409, an average thickness of 15 nm, an average diameter of 5 μm and a surface area of 50–80 m^2/g. All elemental powders and GNPs are utilized without further purification.

2.2. Preparation of GNPs/IN738 composite powder

Due to variations in the density of the elemental powders and GNP, a 3D high-speed turbula mixing shaker is used to pre-alloy the powder to ensure the homogenous dispersion of powder particles. Hard W balls were added to the green powder during pre-alloying and mixing to aid homogeneity and prevent the formation of agglomerates. The balls are added at a ratio of 10:1. Prior to powder mixing, a digital weighing balance with an accuracy of $\pm$ 0.01 mm is employed to measure individual powder (element and GNP) in a vacuum hand glove box. The box ensured that the powders were protected from reacting with the environment (mainly air and oxygen). Ethanol is used to rinse the W balls and left to dry (30 min) before adding them to the powders. This is done to ensure that impurities are prevented from contaminating the body of the green powder. The elemental powders and GNPs were poured into a plastic container and carefully placed in the turbular mixer. The T2F turbula mixer shaker is set at a speed of 110 rpm, and the alloying/mixing process is conducted for 8 h in a dry environment. The elements that make up the composite powder are of different shapes and sizes, targeted at improving powder compaction and densification. The admixed powder has a theoretical density of 7.911 g/cm^3. In order to make sure that homogenous mixing is achieved, a planetary ball milling (PM 400 MA) machine is employed at a low rotational speed of 101 rpm for 5 h. The operation is performed in the airtight stainless steel 304 L fixture container in a wet media (using ethanol solution) coupled with the inclusion of W balls at a ratio of 10:1, ball to powder ratio, to ensure miscibility. Afterwards, the wet powder is moved to the LAB-conco vacuum dryer to dry off the ethanol. The set temperature is 70 °C operated for 6 h. Also, the admixed powders were returned to the turbular mixer to break down any caked or agglomerate that could have formed during drying at 70 °C. Tungsten balls were equally utilized in the process. Table 1 summarises the elemental powder weight percent of GNPs/IN738 composite.

2.3. Spark plasma sintering of GNPs/IN738 composite

At the completion of the mixing operation, the composite powder is transferred to the prepared graphite die in readiness for sintering. The graphite die employed has an external diameter of 60 $\pm$ 0.1 mm, an internal diameter of 40 $\pm$ 0.05 mm and a height of 48 mm. The interior of the graphite die,

Table 1 – Wt.% of starting powders for the synthesizes of GNPs/IN738 composite.							
Materials	Ni	Cr	Ti	W	Co	Ta	Al	GNP
Weight (%)	64.33	16	3.4	2.6	8.3	1.72	3.4	0.25

including the surface of the two punches that made contact with the composite powder, was lined with 0.2 mm thick graphite paper. This is necessary to ensure easy removal of the sintered composite from the graphite die/punches (mould) after sintering. Subsequently, the graphite die holding the admixed powder is placed in the heating chamber of the SPS machine (model HHPD-25, Germany). The column of the SPS furnace chamber consists of graphite die equipped with eight spacers and two plungers. The environment of the heating chamber is maintained at 0.5 mbar vacuum pressure and absolute pressure of 1.2 mbar to prevent oxygen contamination during sintering. The fabrication processes were designed to sinter 40 × 6 mm test samples (diameter by thickness), and the total mass of admixed powder (composite) required is 59.4 g. This was measured and poured into the graphite die. The composite samples were sintered at the sintering temperature of 900, 1000, 1050 and 1100 °C, a pressure of 50 MPa, heating rate of 100 °C/min and soaking time of 5 min. After the sintering processes, when the set temperature, pressure, heating rate and holding time have been achieved, the current is switched off to allow the sintered composite to cool. The sintered sample is ensured to cool to ambient temperature (22 °C) in the furnace before removing it. The sintering process is repeated to obtain the desired number of samples. Due to the effect of graphite paper used as insulation (between the graphite die and composite powder), traces of graphite were deposited on the surface of the sintered material. This is regarded as an impurity on the surface of the material and was sandblasted. However, it does not affect the microstructure of the sintered composite. The sintered materials were metallographically prepared for further investigation.

2.4. Density and microhardness processes of GNPs/IN738 composites

The theoretical bulk density of the composite powder is calculated according to the equation obtained from the literature [17]. The experimental relative densities of the sintered composites were measured by using the Archimedes principle method. In contrast, the rule of the mixture is employed to compute the relative densities of the sintered composite with respect to the theoretical density of the composite. The experimental density was measured over ten trials using an electric densimeter with an accuracy of ± 0.0001g, and the average was taken to represent the original relative density value. This is done to ensure that accurate reading capturing the original value of the experimental density is utilized. The microhardness property of the sintered composites is investigated using Vicker's microhardness (HV) tester machine (Future-tech, 800). A diamond indenter is used with a load of 1000 gf (1.0 N), a dwell time of 15 s and a spacing of 0.1. The process is repeated ten times for each sample at room temperature (RT). The arithmetic means of the successful indentation is calculated and recorded as the original microhardness value of the material.

The points indented were selected from different grains representing different phases, grain boundaries and solid solution phases observed on the microstructure to reflect the actual hardness property of the material. A similar procedure is followed during nanoindentation analysis on mounted and polished (mirror-like surface) samples according to ASTM D785 standard [28]. The load of 100 mN with a loading and unloading time of 25 s and a holding time of 10 s were employed. An average of six indents are captured per sample, and the mean average is calculated to represent the sample's actual nanohardnesse value. The nanoindentation machine has a diamond Berkovich pyramid indenter (three-sided). Subsequently, Oliver and Pharr's method is employed to evaluate the Young's modulus (GPa) and nanohardness (GPa) of the sintered GNPs/IN738 composite sample using the precise equations as illustrated by Okoro et al. [29]. And Dada et al. [30].

2.5. Microstructure characterization GNPs/IN738 composite

The morphology of the GNPs/IN738 composite sintered at a temperature of 900, 1000, 1050 and 1100 °C and their corresponding wear scar after wear analysis are characterized by field emission scanning electron microscopy (FE-SEM Zeiss Ultra Plus 55) incorporated with an energy dispersive spectroscopy (EDS) detector. The SEM is operated at 1.0 kV accelerating voltage. The morphology in terms of grain size, shape and boundaries of the sintered composite is further analyzed by examining the area of the grains in different paths to calculate the grain size dispersion through the application of *ImageJ graphics software*. The strengthening phases developed were identified utilizing the PANalytical Empyrean X-ray diffraction (XRD) applying a scan rate of 0.02 °/sec, CuK α radiation (λ) of 0.154 nm, accelerating voltage of 50 kV and 30 mA electric current over the angular range of 10—90 °. Raman spectroscopy analysis is achieved using a T64000 micro-Raman spectrometer (HORIBA Scientific, Jobin Yvon equipment. A laser wavelength of 514 nm and 120 s spectral acquisition time were used for the operation. Subsequently, six locations representing the position of GNPs were captured for the Raman spectra to ensure data accuracy. The Raman shift representing the D and G bands are calibrated according to the ASTM E1840-96 standard [31].

2.6. Wear analysis of GNPs/IN738 composite

The dry wear analysis of the GNPs/IN738 composite sintered at varying temperatures from 900 to 1100 °C is assessed at 25 °C room temperature (RT) employing an Anton Paar, TTX-NHT[3] tribometer following ASTM G99-95 standard. The analysis is performed by applying a pin-on-disc dry-sliding rotating wheel outfitted with a wear and friction data recording system. Parameters and counterface specifications include a rotating speed of 300 rpm, a load of 5, 10 and 20 N at 30 min each (analysis time), and a stainless-steel pin counterface with a 1 mm diameter tip and a roughness (Ra) of 0.03 mm. This is performed without aiding lubrication, and they are sufficient to produce good wear performance. The process design requires that the counterface be placed stationary on the exposed surface of the pre-fixed test sample, which is mounted axially on a rotating wheel that unidirectionally slides when in operation. At the completion of the process, the wear rate and the coefficient of friction recorded against the sliding time were captured and recorded by the

monitoring unit (system). Particularly, the wear rate is captured through the profilometer (Surtronic S128) fastened to the tribometer machine. Therefore, the wear rate is recorded by measuring the worn surface profile produced by plastic deformation.

### 2.7. *Laser flash analysis of GNPs/IN738 composites*

The thermophysical properties in terms of the thermal diffusivity, thermal conductivity, and specific heat capacity of the sintered GNPs/IN738 composites from RT to 600 °C are investigated using a Netzsch LFA 457 Hyperflash [32]. A sample of $10 \times 10 \times 5$ mm thickness is used for the analysis. The relative density of the sintered samples measured through the Archimedes techniques is supplied for each sample. The heat transfer is evaluated in the high temperature water-cooled furnace chamber of the machine accompanied with nitrogen to create an inert environment during analysis. A graphite spray is applied on the test sample's exposed flat surfaces (both sides) to ensure even absorption of the laser flash energy. In the analysis, pulsed energy released from the laser is made to strike the sample's sprayed surface (one side) utilizing a laser voltage of 450 V at a pulse rate of 0.8 ms. The samples were evaluated from RT to 600 °C at an interval of 100 °C. The sintered GNPs/IN738 composite test samples were able to absorb the heat because of the thermal conductivity enhancement provided by the graphite spray and the good thermal conductivity quality of the test sample. At the attainment of each desired temperature, the laser is flashed

three times, and the average mean value is taken to represent the true value measured. The thermal diffusivity values were recorded after the heat diffused through the sample using the IN-Sb detector in relation to time. The thermal conductivity for each measured sample is evaluated by multiplying the relative density of the composite sample with the specific heat capacity and thermal diffusivity value, all computed using the software on the computer monitoring system attached to the LFA machine.

3. Results and discussion

3.1. *Microstructure analysis of GNPs/IN738 composites*

The SEM morphology of the sintered GNPs/IN738 composites at different sintering temperatures of 900, 1000, 1050 and 1100 °C are shown in Fig. 1a–d to understand the microstructural features. The micrographs show the presence of minimal pores with the admixture of different phases denoted with different colours. Also, the percentage porosity reduces with the increasing sintering temperature, and the relative density measurement corroborates this observation. The sample sintered at 900 °C displays apparent porosity, which fizzles with the rising sintering temperature. The phases present appears to be heterogeneously dispersed with different grain sizes in the microstructure of the sintered composites, and they are characterized using EDS. According to the EDS analysis, the dark grey spot represents the solution of both gamma
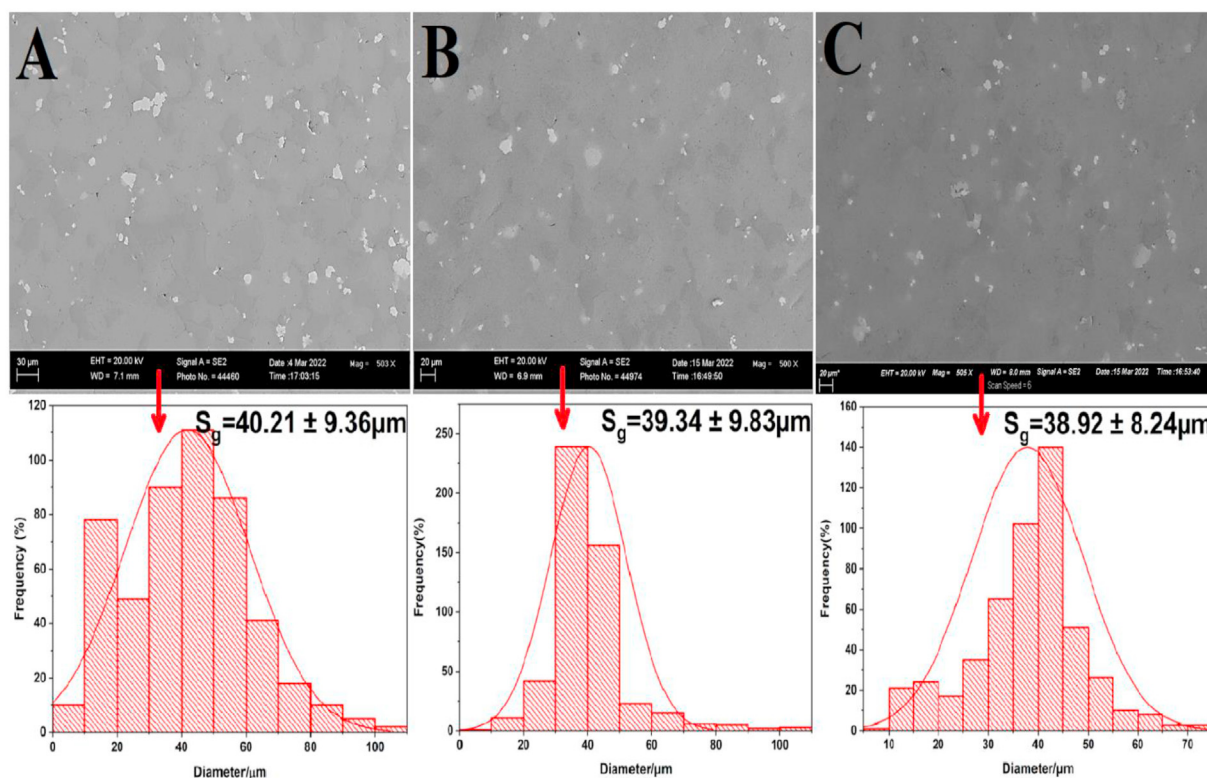
Fig. 1 — The micrographs, grain size distribution and EDS of the sintered GNPs/IN738 composites at varied sintering temperatures. (a) 900 °C, (b) 1000 °C, (c) 1050 °C, (d) 1100 °C.
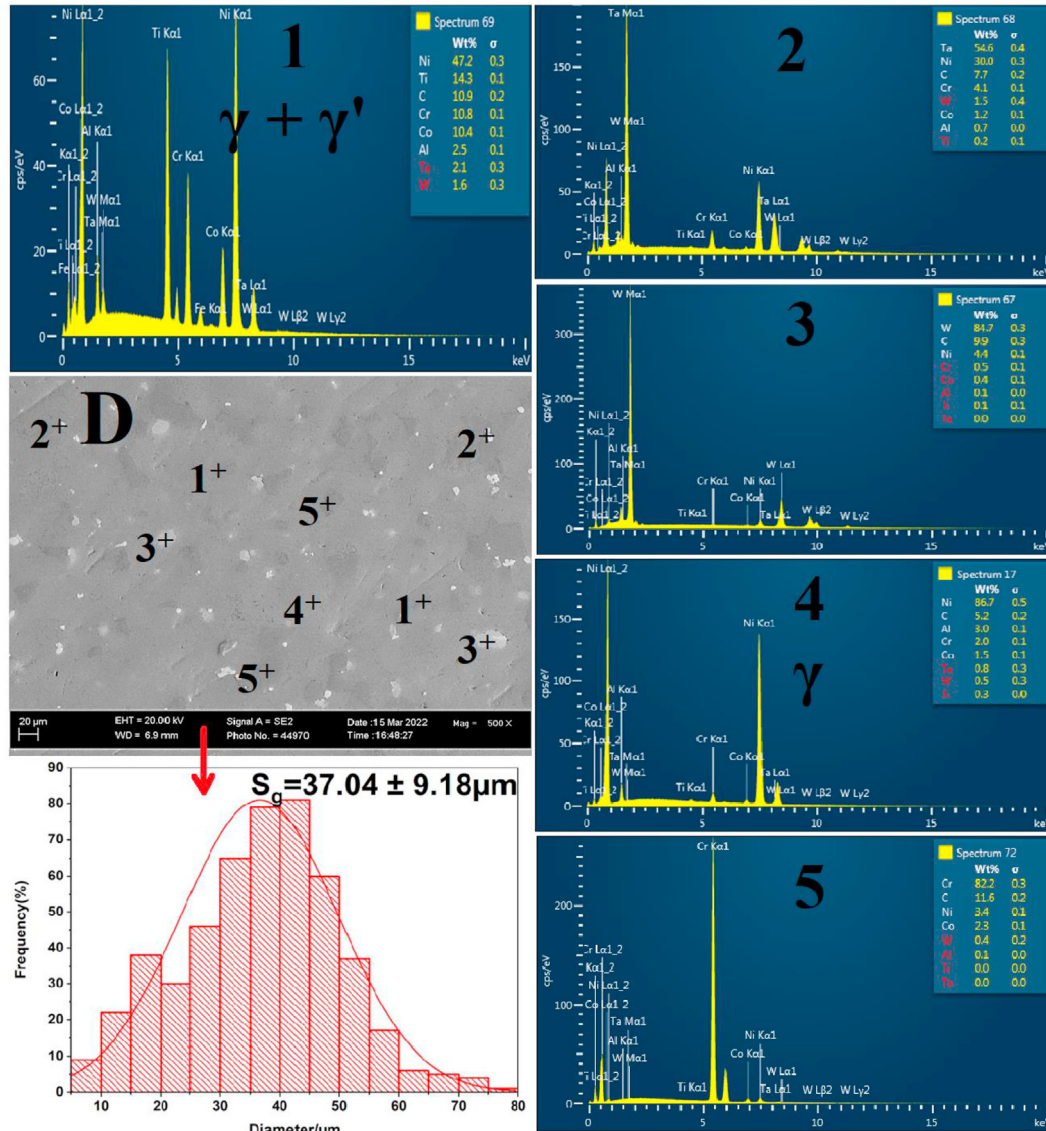
Fig. 1 — continued

(γ) and gamma prime (γ′) phase, and the light grey spot represents the gamma (γ) matrix phase, while the whitish spot is a combination of different solid solution (W,Cr,Ta) strengthening phases. These features were typical characteristics of Ni-based superalloys, and the gamma matrix phase is formed in all the samples due to the high presence of Ni element [32]. The intermetallic gamma prime (Ni₃Al and Ni₃Ti) phase is developed due to the diffusional reaction that occurs at high sintering temperature between the matrix Ni and Al/Ti alloying elements and its precipitate within the matrix gamma phase (identical lattice parameters). The W, Cr and Ta precipitate, as a solid solution strengthening phase, impact the strength of the composites. The EDS analysis implies that the gamma and gamma prime phases overlapped in their formation and is ascribed to their matching and identical crystal structures (face center cubic). Thus, they are frequently developed on the same crystallographic plane

within Ni-based alloys [33]. The precipitates gamma prime and solid solution strengthening phases contribute significantly to the mechanical properties of the sintered composites aside from the contribution of graphene nanoplatelets. It is noteworthy that graphene nanoplatelets' agglomeration traces are not apparent from the SEM micrographs. The EDS spectrum confirms the presence of carbon, suggesting that graphene is present because it is an allotrope of carbon. Shuan et al. [21] indicated that the volume of graphene constituent in Ni-based matrix superalloy impacts the intensity of the peak formed in the EDS spectrum. In this study, the intensity of the peak representing graphene nanoplatelets in the EDS analysis is not conspicuous due to the small amount added.

Given the contribution of graphene nanoplatelets to the sintered GNP-Ni-based composites, grain characteristics (size and distribution) were observed, analyzed, and reported using grain size distribution curves. The grain size analysis and
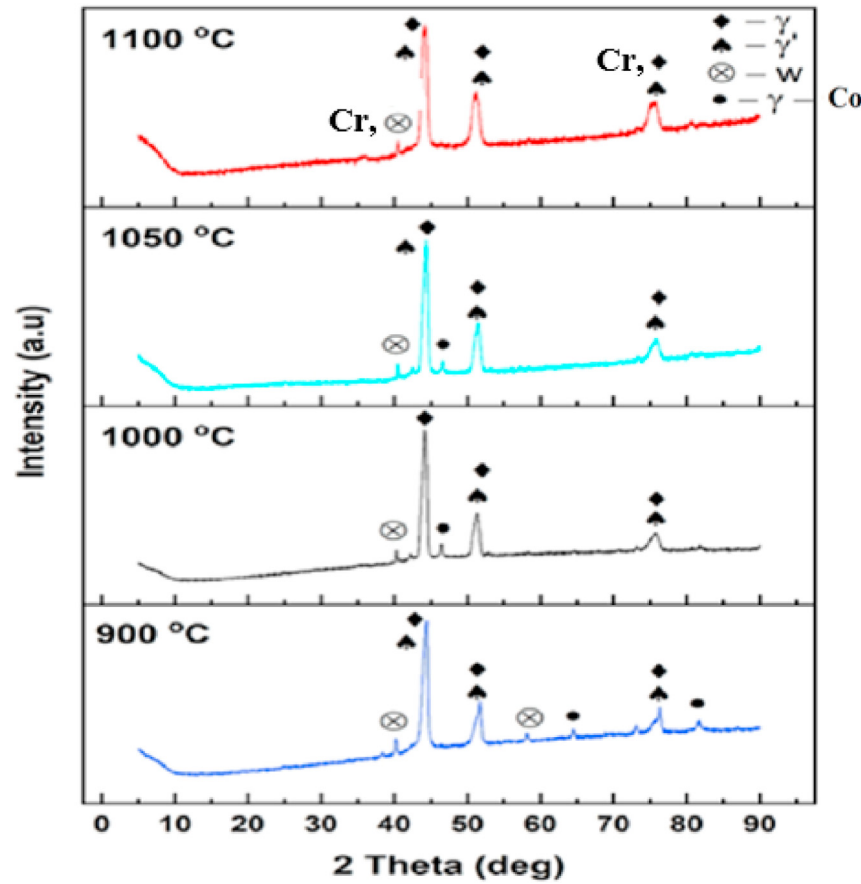
Fig. 2 − XRD patterns of the sintered GNPs/IN738 composites at varied sintering temperatures. (a) 900 °C, (b) 1000 °C, (c) 1050 °C, (d) 1100 °C.

distribution map is attached to the micrograph of each sample pointed with the red arrow. The microstructures of the sintered GNPs-Ni-based composites display a uniform coarse grains structure with decreasing average grain size as the sintering temperature increases. As the sintering temperature increases from 900 to 1000, 1050 and 1100 °C, the average grain size of the GNP-Ni-based composites decreases from 40.21 to 39.34, 38.92 and 37.04 μm, respectively. This demonstrates that the in-situ GNPs reinforcement can induce a grain refinement phenomenon (promoting grain nucleation) in the Ni-based matrix alloy [11].

Meanwhile, grain refinement formation may be ascribed to the pinning effect produced by GNPs at the grain boundaries. The homogenous dispersion of GNPs during powder mixing contributes to the inhibition of grain growth of Ni matrix during the sintering process, and in addition, the GNPs reinforcement act as heterogeneous nucleation sites for new grains [34,35]. The remarkable grain refinement effect of GNPs as reinforcement in Ni-based composites has been elucidated in literature [15,34,36], whereabouts the refined grains perform a vital role in improving the mechanical properties. Summarily, no obvious crack is observed; however, the minimal pores present reduce as the sintering temperature increases, thus, implying that the SPS process fully consolidates the bulk materials.

3.2. X-ray diffraction analysis of GNPs/IN738 composites

The XRD patterns of the sintered GNPs/IN738 composites at different sintering temperature of 900−1100 °C is shown in Fig. 2. Three major and intense diffraction peaks were obvious in all the samples appearing at 44.7°, 52.1° and 75.9° 2 theta angle of diffraction. These peaks are indexed to the (111), (200) and (220) crystalline planes of the face-centered cubic structure of Ni [37]. Even though graphene is present in the composites, no traces of impurity diffraction peaks associated with the nickel carbides are noticed, signifying the formation of an orderly and stable GNPs/Ni interface devoid of any observable chemical reaction. The major peaks comprise an overlapping formation of gamma matrix and gamma prime intermetallic phases (Ni_3 (Ti, Al)) while solid solution phases (Cr, W) appear on the minor peaks, thus corroborating SEM/EDS analysis. These phases are formed due to a chemical reaction between matrix and alloying elements assisted with the application of high heat energy.

It is noticed that the minor peaks comprising W and Co precipitate solid solution fizzle out and decompose with the increasing sintering temperature, whereas Cr remains, therefore suggesting that high sintering temperature reduces W/Co precipitate and promotes diffusion [32]. The diffraction

peaks' position, intensity and shape remain almost the same in all the samples, indicating no formation of prior texture in the composites after SPS [38,39]. The metallurgical observation is similar to the reported studies documented in the literature [40]. On the other hand, the diffraction peak corresponding to the presence of GNPs is not detected from the XRD pattern, which may be due to the relatively low concentration added [41]. Consequently, further analysis is imperative to identify the formation and behaviour of GNPs in the GNPs/IN738 composites at different sintering temperatures of 900–1100 °C. Thus, Raman spectroscopy is used to investigate the microstructure of the sintered composites at different sintering temperatures.

3.3. Raman spectroscopy analysis of GNPs/IN738 composites

As shown in Fig. 3, the Raman spectra of the sintered GNPs/IN738 composites at varied sintering temperatures from 900 to 1100 °C are displayed, and the corresponding data are presented in Table 1. Three main peaks corresponding to the D-band peak at 1349 cm^{-1}, G-band peak at 1583 cm^{-1} and 2D-band peak at 2692 cm^{-1} of graphene nanoplatelets can be observed in the spectrum of the Raman analysis [42]. The D-band mode of GNPs is conspicuously suggesting the formation of sp3 carbon and defects. The G-band mode is related to the first-order scattering of E_{2g} phonons associated with the in-plane straightening mode of sp^2-bonded carbon in a two-dimensional hexagonal lattice. Meanwhile, the 2D-band mode is obtained from the double-resonant scattering of electrons and holes from phonons involving states positioned on the Dirac cones at the K-points [43]. Notably, the 2D band is only obvious in the composite sintered at 900 °C. Also, the number of graphene layers in the composites determines the height and position of G and 2D band peaks, and the intensity ratio between 2D and G modes can be utilized to analyze the grain size and the number of layers of graphene formed. The grain size of graphene could not be evaluated in this study because the 2D peak is not apparent in all the samples.

Furthermore, the evaluation ratio of the intensity of the D and G band (I_D/I_G) describes the integrity of the structure or
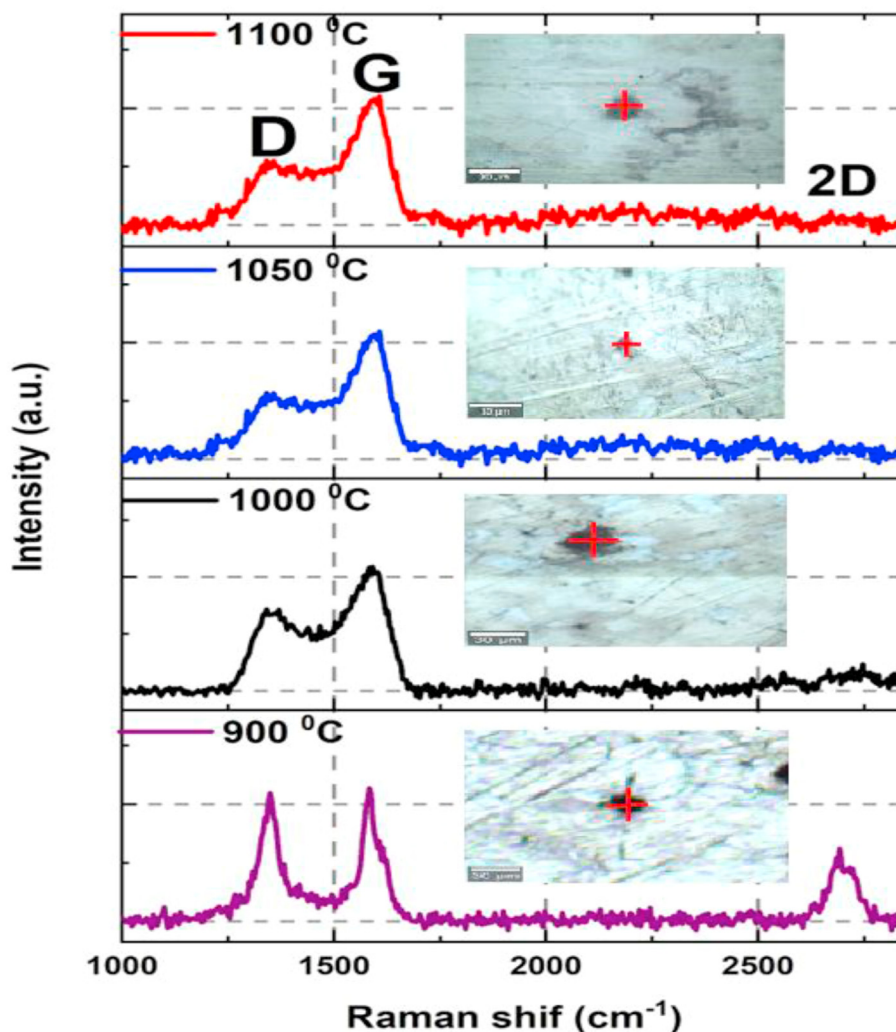

Fig. 3 – Raman spectra of the sintered GNPs/IN738 composites at varied sintering temperatures. (a) 900 °C, (b) 1000 °C, (c) 1050 °C, (d) 1100 °C.

possible defect that might be developed during the distribution of GNPs in the IN738 alloy. Therefore, the evaluated value of the I_D/I_G of the sintered composites at 900 to 1100 °C are 0.96 (900 °C), 0.66 (1000 °C), 0.52 (1050 °C) and 0.51 (1100 °C), respectively. At low sintering temperatures, there is an accumulation of non-sp2 defects in the graphitic structure of GNPs during its distribution. The defect frequently presents as vacancies and broken edges in GNPs grains [44]. The high value ratio of I_D/I_G of GNPs (0.96) obtained in the composite sintered at 900 °C indicates that carbon graphitization is developed, and the low values of I_D/I_G ratio at high sintering temperature imply that graphitization of carbon is less pronounced during sintering. It suggests that the SPS process induces graphitization-healing of GNPs with the increasing sintering temperature [42,45]. Thus, the microstructure of the composite sintered at high sintering temperature is well refined, leading to properties enhancement. The vacancies present in the microstructure of the composites are occupied and rearranged in their graphitic structure. Accordingly, the matrix atoms may have filled the pores present within the structure of GNPs by infiltrating the carbon layers during sintering, leading to a lower ratio of I_D/I_G value obtained with composite sintered at high temperatures (1050 °C and 1100 °C) compared to those at low temperatures (900 °C and 1000 °C).

3.4. Microhardness, relative density, nanohardness, and elastic modulus measurements of the sintered GNPs/IN738 composite at different sintering temperatures from 900 to 1100 °C

The effects of varied sintering temperatures on the spark plasma sintered GNPs/IN738 composite with respect to the microhardness, relative density, nanohardness and Young's modulus are shown in Fig. 4, and their corresponding data are presented in Table 3. It is observed that the microhardness, relative density, nanohardness and elastic modulus increase with the increasing sintering temperature. The microhardness increased from 354 HV at 900 °C sintering temperature to 469 HV at 1100 °C, nanohardness from 8.2 to 17.9 GPa, relative density from 94.79% to 98.53% and Young's modulus from 190 to 291 GPa, respectively. The highest relative density of 98.53% obtained at a sintering temperature of 1100 °C implies that the microstructure of the sintered GNPs-IN738 Ni-based composite is appropriate for SPS consolidation and upwardly improves the mechanical properties. Thus, high sintering temperatures may accelerate the densification and consolidation of GNPs/IN738 Ni-based composite powder. The significant increment in relative density with the increasing sintering temperature suggests that sintering temperature substantially influences densification [46]. In addition to the contribution of the high relative density that leads to higher hardness is the formation of gamma matrix, intermetallic gamma prime, precipitate hard solid solution strengthening phase and GNPs reinforcement that improves the mechanical properties of the composite [33]. Consequently, the SPS technique promotes the diffusion of atoms, formation of grain and strong metallurgical bond, which improves the strength of the sintered GNPs-IN738 Ni-based composite.

3.5. Load-depth and depth–time curves of the sintered GNPs/IN738 composite at different sintering temperatures from 900 to 1100 °C

The nanoindentation load-depth (with insert showing the enlarged view up to 15 mN load to highlight the pop-in effect (pointed with arrow)) and depth–time curves of the sintered GNPs/IN738 composite at different sintering temperatures from 900 to 1100 °C utilizing an indentation load of 100 mN are illustrated in Fig. 5a and b. Observing the pattern produced after the analysis (indentations) shows that the responses are similar comparing the loading and unloading curves. There is evidence of pop-in effects in all the sintered samples under the load of 100 mN, which may be attributed to the transfer of strain and formation of dislocation at the surrounding grain boundaries in the microstructure of the composites. Thus, this impedes against dislocation motion forced by the indentation [30]. The load-depth curves illustrate the formation of an elastic–plastic deformation performance, and it is evident that the composite sintered at 900 °C displays the highest penetration depth, followed by the composite sintered at 1000 °C up to that of 1100 °C. This implies that the penetration depth reduces with the increase in sintering temperature. Couple with the positive influence of sintering temperature is the presence of hard precipitate solid solution and GNPs that assist in improving the resistance of the sintered GNPs/IN738 composite to plastic deformation during indentation.

Similarly, the penetration depth against time curves for the GNPs/IN738 composite sintered at temperatures between 900 and 1100 °C, analyzed under 100 mN, is displayed in Fig. 5b. The curve further confirms the existence of high plastic deformation in all the tested samples. By comparing the four composite samples, the maximum penetration depth is observed in the composite sintered at 900 °C followed by the sample sintered at 1000 °C up to that of 1100 °C, thus implying that the penetration depth reduces with increasing sintering temperature. The penetration depth value of the composite sintered at 900, 1000, 1050, and 1100 °C correspond to 673.23, 606.32, 529.52, and 427.37 nm. Accordingly, this behaviour signifies that the micro/nano hardness, stiffness and elastic modulus of the sintered composite are enhanced through the formation of gamma, gamma prime, and precipitate solid solution phases (aided by vigorous diffusion at high sintering temperature). Coupled with the phases mentioned is the presence of GNPs with high mechanical properties that contribute equally to the improvement of strength in the composites. Finally, the depth–time curves are similar for all the GNPs/IN738 composite samples.

3.6. Wear behaviour of sintered IN738LC-GNPs Ni-based composites

3.6.1. Coefficient of friction behaviour of GNPs/IN738 composite sintered at different sintering temperature from 900 to 1100 °C

The coefficient of friction (COF) performances of the GNPs/IN738 composite alloy sintered at different sintering temperatures from 900 to 1100 °C are illustrated in Fig. 6 under three
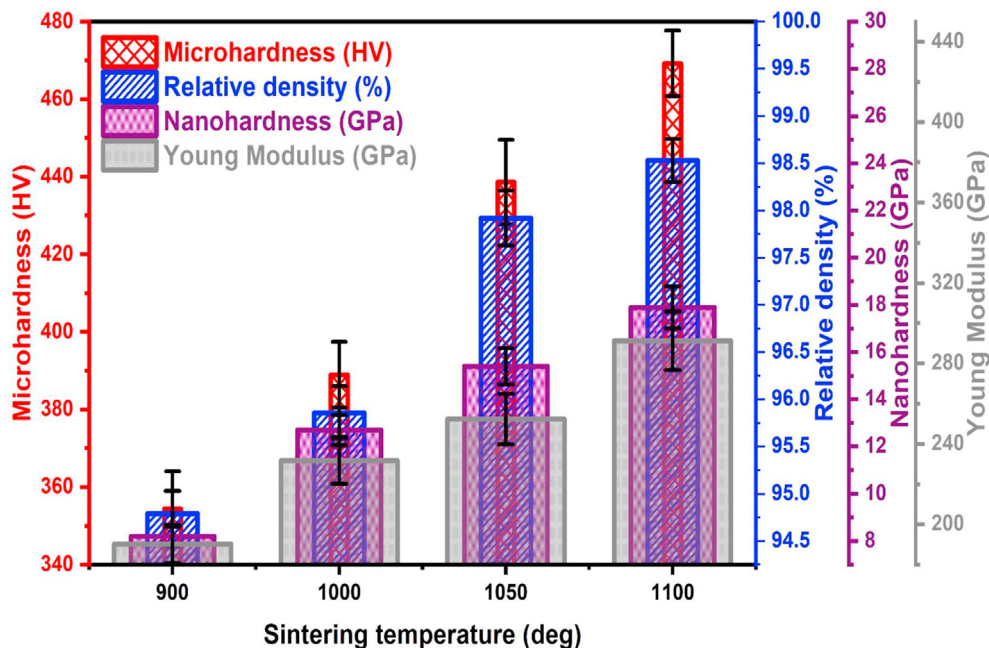
Fig. 4 – Microhardness, relative density, nanohardness and Young's modulus of the sintered GNPs/IN738 composites at varied sintering temperatures from 900 to 1100 °C.

testing loads of 5, 10 and 20N, respectively. The COF responses are plotted against a sliding time of 30 min. The COF patterns display three distinct phases: running-in, stable, and unstable. However, the three stages were not present for all the loads and the four composite samples. The applied load of 5N shows the running-in and stable state mode, while the applied loads of 10 and 20N display the three stages. The running-in state progressed for a short time under an applied load of 5N and became stable after about 100 s for the sample sintered at 900, 1000 and 1050 °C. The stable state begins about 300 s after the commencement of the analysis for the composite sample sintered at 1100 °C. Thus, the COF behaviour largely depends on the characteristic of the material. The vigorous action of

the steel ball at the point where it made contact with the composite material at the beginning of the testing results in the formation of the running-in state. The stable state stage progressed immediately after the running-in state and continued throughout the testing for the 5N applied load. On the other hand, the wear characteristic under the applied load of 10 and 20 N behaves differently, displaying severe wear activities. The occurrence of running-in, stable and unstable state stages indicates the high level of abrasive and adhesive wear activities, especially at the unstable state stage (COF pattern). The unstable state is commonly caused by the impact of the trapped and accumulated wear debris on the counter load [47,48].
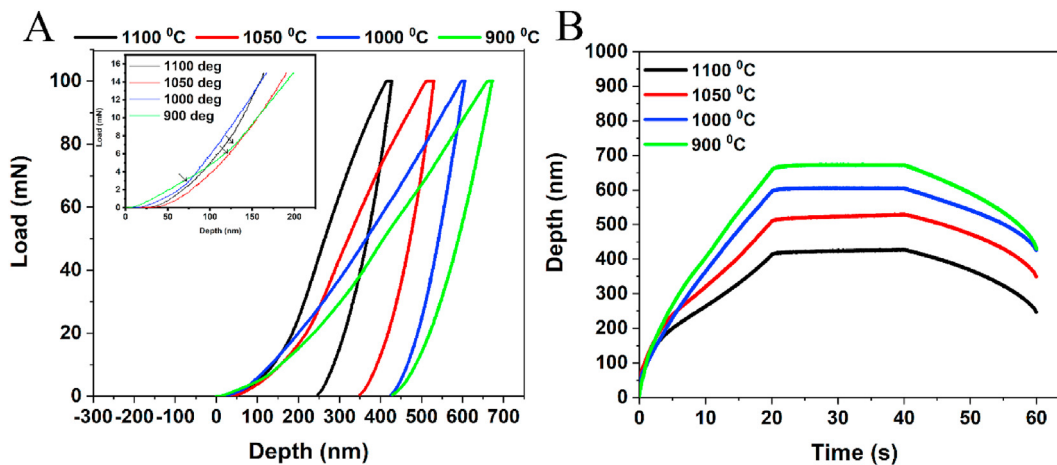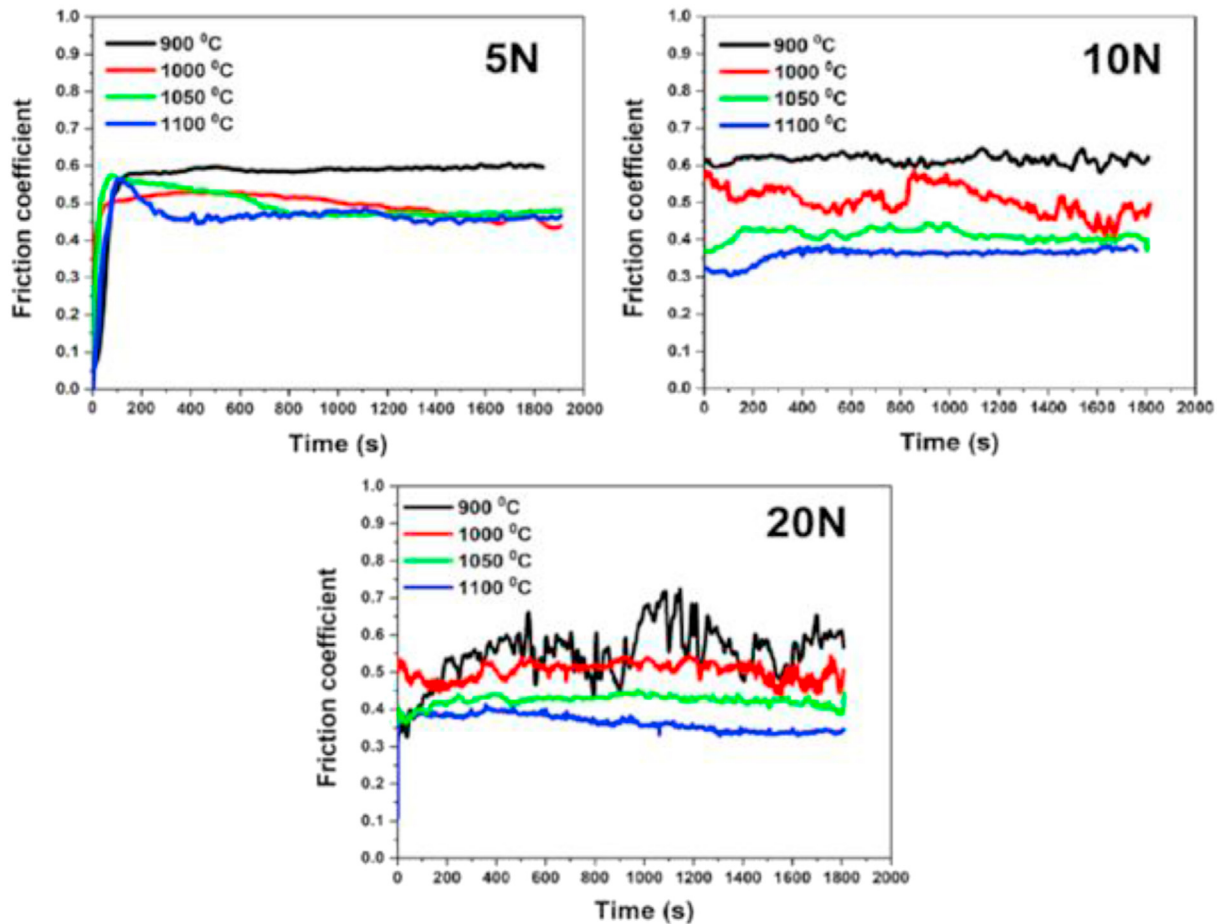

Fig. 5 – a and b. Load-depth (with insert showing the enlarged view up to 15 mN load to highlight the pop-in effect) and Depth-time curves of the sintered GNPs/IN738 composites at varied sintering temperatures from 900 to 1100 °C under an indentation load of 100 mN.
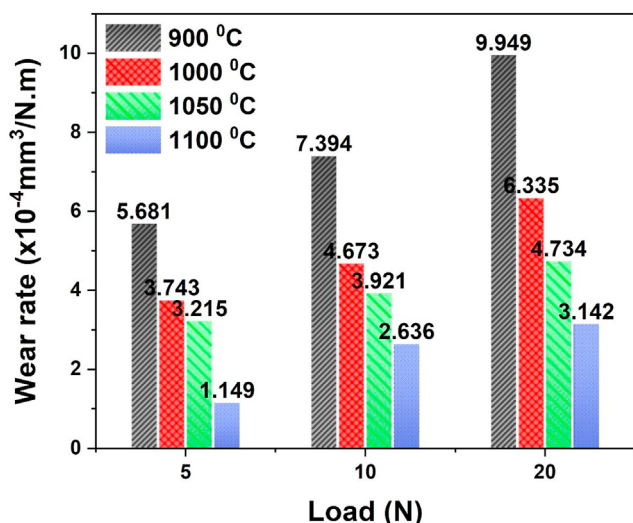
Fig. 6 – The friction coefficient against the time of the sintered GNPs/IN738 composite at varied sintering temperatures from 900 to 1100 °C under loads of 5N, 10N and 20N.

It is observed that the values of the COF reduced with the increasing sintering temperature, suggesting that the inherent increased hardness strength caused by high densification, resulting from atom diffusion at the high sintering temperature, impacted the COF responses. The measure of the steadiness of the steady(stable) state phase witnessed for all the sintered materials at a 5 N low applied load is associated with the behaviour of the fine protective oxide layer formed during adhesion and abrasive wear reaction. Consequently, the protective oxide layer is capable of surviving the pressure exacted by the applied load within the time of the experimentation. While this is so, Belmonte M. et al. [49], submitted that the presence of graphene nanoplatelets reinforcement in the metal matrix could result in the formation of a graphene-based tribofilm during wear testing, and it can impact the responses of the wear of a material. Therefore, the appearance of the tribofilm could equally contribute to the formation of the unstable state phase utilizing a high load of 10 and 20 N. Although, the extent of its contribution could not be ascertained at this stage. Overall, the applied load of 5N display two stages, namely the running-in stage at the beginning of the analysis and the stable state, which is maintained throughout the experimentation. At the completion of the testing, the sample sintered at 900 °C had the

highest COF average value, while the one sintered at 1100 °C displayed the lowest average value of COF. High loads of 10 and 20 N display similar characteristics, with samples sintered at 1100 °C showing the least average COF while samples sintered at 900 °C display the highest average COF. Coupled with the influence of sintering temperature on the responses of GNPs/IN738 composite is the distribution of phases present within the microstructure and the behaviour of the oxide layers produced. The heterogeneous distribution of phases in the microstructures of the sintered composites (independent of the relative density), especially the precipitate solid solution phase coupled with the mechanical action of the steel ball counterface during wear testing (rotational motion), could result in the continuous formation and rupture of friction reducing layer. Thus, resulting in the formation of an unstable state phase [50,51].

3.6.2. Wear rate of GNPs/IN738 composite sintered at different sintering temperatures from 900 to 1100 °C

The wear rate of GNPs/IN738 composite sintered at different sintering temperature from 900 to 1100 °C is revealed in Fig. 7. The wear rate of the Ni-based composite sintered at the least sintering temperature of 900 °C shows the highest wear rate under the three varied loads of 5, 10 and 20 N. The values
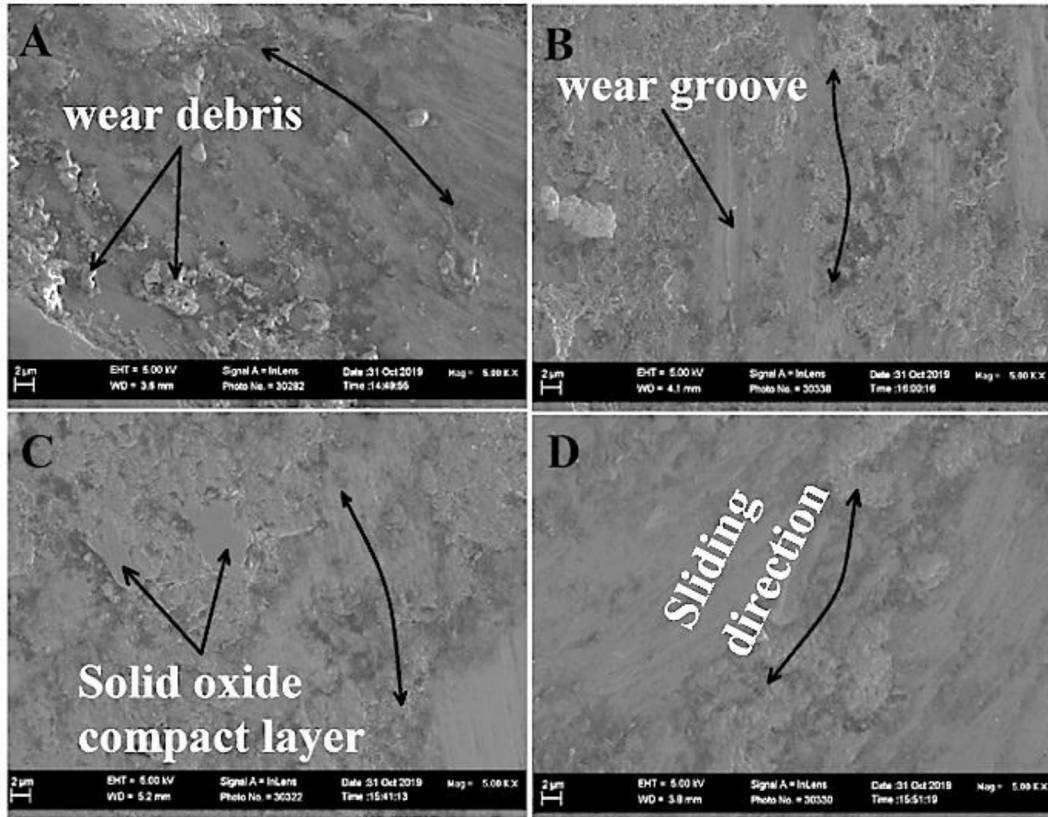
Fig. 7 — The wear rate of the sintered GNPs/IN738 composites at varied sintering temperatures from 900 to 1100 °C under loads of 5, 10 and 20N.

recorded for the increasing loads were 5.681×10^{-4}, 7.394×10^{-4} and 9.949×10^{-4} mm^3/Nm, respectively. Also, it is observed that the sintered Ni-based composite with the highest sintering temperature of 1100 °C displays high resistance to wear under the three different loads compared with composites sintered at lower sintering temperatures. The wear rate recorded using 5, 10, and 20 N loads were 1.149×10^{-4}, 2.636×10^{-4} and 3.142×10^{-4} mm^3/Nm, respectively. Similarly, the composites sintered at 1000 and 1050 °C display similar results under the three varied loads. The wear rate obtained were 3.743×10^{-4}, 4.673×10^{-4} and 6.335×10^{-4} mm^3/Nm for composite sintered at 1000 °C and 3.215×10^{-4}, 3.921×10^{-4}, and 4.734×10^{-4} mm^3/Nm, respectively for composite sintered at 1050 °C, at the varied load of 5, 10 and 20N. It is apparent that the wear rate reduces substantially with the increasing sintering temperature. The wear resistance of the sintered GNPs/IN738 composite is mainly ascribed to the effect of relative density and hardness property [52].

Accordingly, this study indicates that the hardness property of the sintered composites increases with the increasing sintering temperature, thereby increasing the wear rate. There is a 79% decline in the wear rate between the composite sintered at 900 °C and 1100 °C under 5 N applied load. Subsequently, the same observation is noticed using the applied load of 10 and 20 N, recording a 64% (10 N) and 68% (20 N) reduction in wear rate between the composite sintered at 900 °C and 1100 °C. Aside from the pronounced influence of sintering temperature, which contributes to the increase in the mechanical properties of the composites, the addition of GNPs reinforcement is thought to contribute to the improvement in the tribological performance of the materials. Also, and as observed with the mechanical properties, the improved wear resistance of the sintered composites could be attributed to the formation of the dominant gamma phase, the presence of precipitate intermetallic gamma prime (Ni$_3$(Ti, Al) phase and the precipitate hard solid solution phase. The intermetallic

gamma prime (Ni$_3$(Ti, Al) phase often develops at the same position as the gamma matrix phase and stimulates a self-lubrication effect during wear testing leading to high wear resistance and improved wear properties. Therefore, the improvement in the wear resistance behaviours of GNPs/IN738 composite are summarized as follows: the contributing influence of nanofiller GNPs, the formation of strengthening intermetallic and precipitate hard phase solid solution phases [37].

3.6.3. Worn surface analysis of GNPs/IN738 composite sintered at different sintering temperature from 900 to 1100 °C

The SEM images of the worn track after sliding wear analysis of GNPs/IN738 composite sintered at different sintering temperatures from 900 to 1100 °C are shown in Fig. 8a—d. The worn track of the tested composite demonstrates the presence of grooves and delamination accompanied by wear debris appearing as flakes. The composites produced at 900 °C sintering temperature (Fig. 8a) had more noticeable delamination and solid oxide layer formation, indicating the severity of the wear activities. A damaging abrasive wear behaviour on the worn surface occurs. However, the formation of grooves, delamination and wear debris are noticed to reduce with the increasing sintering temperature for Fig. 8b (1000 °C), 8c (1050 °C) and 8d (1100 °C). A relatively smooth worn track with shallow grooves and reduced solid oxide layers were observed in these samples. It is observed that the solid oxide formed prevents severe wear damage by serving as a protective barrier on the worn surface of the sintered composites, thus, reducing the wear rate. The smother surface achieved signifies that plastic deformation and temperate abrasive wear are the two prevailing wear mechanisms that take place with increasing sintering temperatures. According to Xiao W. H et al. [41], the GNPs and intermetallic gamma prime phase possess self-lubricating characteristics, which contributes to the reduction in the wear activities of the sintered GNPs/IN738 composites. Coupled with the significant contribution of sintering temperature to the relative density of the sintered composite leading to the development of good mechanical properties is the contribution of the GNPs reinforcement which contributes to the increased hardness property. In so doing, under a sliding contact surface (steel ball), GNPs inhibit the sintered composites from suffering from excessive flow stress, resulting in reduced plastic deformation. Due to the nano size of GNPs, its addition assists in minimizing the formation and propagation of cracks which are evidently observed from the wear track of the composite [41]. Overall, the inclusion of GNPs is thought to help in the formation of a protective and lubricating oxide layer on the wear track of the sintered composites. As such, the surface of the test samples is protected from experiencing direct contact between the steel ball counter surface and the workpiece, steering the decrease in the wear rate and friction. Zhai et al. [53] alluded that the presence of GNPs in studying the tribological behaviour of metal matrix composite (graphene nanoplatelets/Ni$_3$Al matrix self-lubricating composites) resulted in the formation of tribofilms on the worn surface of GNPs/Ni$_3$Al composites, in the dry sliding wear experimentation. The tribofilms efficiently lower the wear rate and improved the wear resistance of the manufactured composite.

Fig. 8 — SEM micrographs of the wear track of the sintered GNPs/IN738 composites at varied sintering temperatures under 20N: (a) 900 °C, (b) 1000 °C, (c) 1050 °C, and (d) 1100 °C.

3.7. Thermophysical analysis (thermal diffusivity, conductivity, and specific heat capacity) of GNPs/IN738 composites sintered at different sintering temperatures from 900 to 1100 °C

The thermophysical performance in terms of the thermal diffusivity, thermal conductivity, and specific heat capacity of GNPs/IN738 composite sintered at different sintering temperatures from 900 to 1100 °C as a function of temperature is assessed utilizing the laser flash analysis technique illustrated in Fig. 9. The evaluation is conducted from RT to 600 °C, and the isothermal temperature is recorded at 100 °C interval. The relative density (ρ) value for each sample recorded according to the Archimedes principle technique is used during the process. Similarly, the specific heat capacity (C_p) as the temperature increase is assessed based on the temperature difference between the top and bottom faces of the test samples (ΔT) against the time curve (acquired when conducting thermal diffusivity calculation). A superalloy material is utilized as a reference sample. Subsequently, the thermal conductivity of the test samples is evaluated utilizing the formula in equation (1):

$$\lambda = \rho.C_p.a \tag{1a}$$

where λ is the thermal conductivity, ρ represents the relative density of the sintered composite, C_p is the specific heat capacity and a is the thermal diffusivity.

Fig. 9a-**d** shows that the thermophysical properties in terms of thermal diffusivity, conductivity, and specific heat capacity increase with an increase in temperature for all the tested composite samples. Thermal conductivity of the sintered GNPs/IN738 composite reduces with increasing sintering temperature, which may be attributed to the improved strength due to phases present and graphitization of GNPs carbon reinforcement (Table 2: I_D/I_G ratio at high sintering temperature implies that graphitization of carbon is more pronounced). According to Tiwari J.K. et al. [54], it is thought that this observation suggests an improvement in the scattering of phonons at the grain boundaries, which lowers the mean free path of electrons and phonons that negatively affect the thermal transport performance. Although, there is minimal difference in the data obtained for the sample sintered at 1050 and 1100 °C.

A noteworthy deflection in the thermal response (graphs interpreting the thermophysical behaviour) of the thermophysical behaviour during heating at some specific temperature is observed, known as the point of inflection. This is experienced in all the sintered samples; however, more pronounced in the sample sintered at 900 and 1000 °C. For example, the sample sintered at 900 °C experienced inflection at 400 and 500 °C heating temperatures and the sample sintered at 1000 °C experience inflection at 300, 400 and 600 °C isothermals points. Furthermore, the composite sample sintered at 1050 °C and 1100 °C experience inflection at 500 °C and
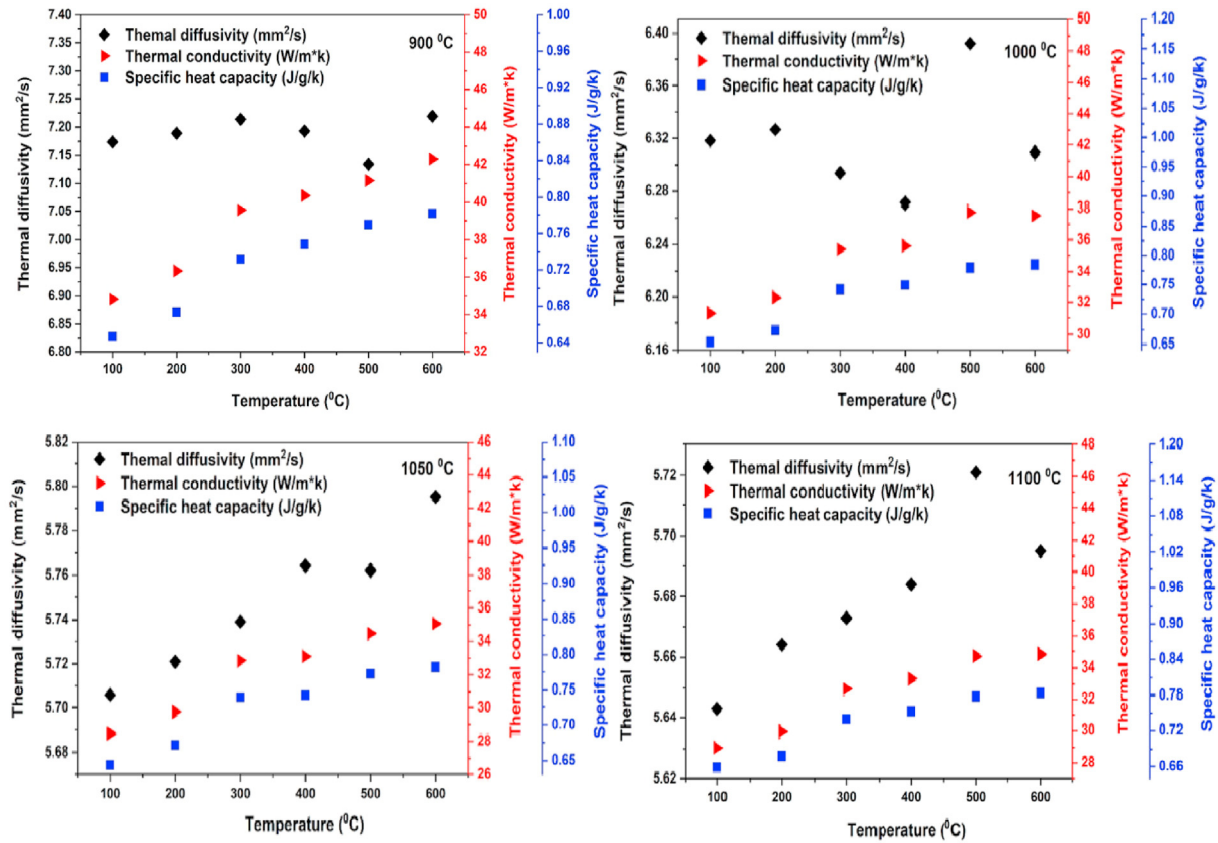
Fig. 9 — SEM micrographs of the wear track of the sintered GNPs/IN738 composites at varied sintering temperatures under 20N: (a) 900 °C, (b) 1000 °C, (c) 1050 °C, and (d) 1100 °C.

600 °C isothermal points, respectively. All the test samples display linear progression in their thermal diffusivity response at the beginning of the increasing temperature before experiencing inflection. It can be inferred that the inflection ensued due to the occurrence of different metallurgical phenomena such as phases transformation (exolution of gamma, gamma prime and solid solution phases) and adjustment within the structure of the materials (atoms rearrangement from the supersaturated Ni matrix and disordering in the matrix phase). More important is the exolution of the intermetallic gamma prime and solid solution phases, which contribute to the linear progression with the increasing temperature of the composites. On the other hand, the dissolution of precipitate intermetallic gamma prime and gamma matrix phases is the phenomenon that ensues at the inflection points leading to a decrease in the thermal

diffusivity as the temperature increase [55]. Additionally, the presence of solid solution Cr (XRD analysis), which form along the grain boundaries in the microstructure of the sintered composites (SEM analysis), is known to form precipitate at a temperature between 477 and 677 °C, thus causing inflection [56]. Although, the inflection started at the temperature of 300 °C in the composite sintered at 1000 °C.

Furthermore, the presence of a few structural defects and internal stress could be responsible for the performance experienced. To understand the behaviour better, Rai A.K. et al. [1] reported in their research that the thermal diffusivity test utilizing LFA may not be sufficient to assert the phenomenon that takes place at the point of inflections. Hence, further analysis employing differential scanning calorimetry (DSC) will be used to further understand the thermophysical properties of GNPs/IN738 composite subsequently. However,

Table 2 — Raman data from the spectra obtained for the sintered GNPs/IN738 composites at varied sintering temperatures (900—1100 °C) and variations in the intensity ratios of I_D/I_G.

Sintering temperature (deg)	Peak Information (y (a.u.) and x (cm^{-1}) axis)			
	D-band	G-band	2D-band	$1_D/I_G$
900 °C	y-273.26, x-1349.20	y-283.37, x-1583.16	—	0.96
1000 °C	y-1925.80, x-1349.20	y-2940.11, x-1583.16	—	0.66
1050 °C	y-29371.70, x-1349.20	y-56917.20, x-1583.16	—	0.52
1100 °C	y-1382.75, x-1349.20	y-2700.20, x-1583.16	y-154-95, x-2692.03	0.51

Table 3 – Microhardness, relative density, nanohardness and Young's modulus of the sintered GNPs/IN738 composites at varied sintering temperatures from 900 to 1100 °C.

Sintering temperature (°C)	Microhardness (HV)	Relative density (%)	Nanohardness (GPa)	Young Modulus (GPa)
900	354.38 ± 9.7	94.79 ± 0.2	8.2 ± 0.4	190.3 ± 9.5
1000	388.98 ± 8.4	95.86 ± 0.3	12.7 ± 0.6	231.8 ± 11.6
1050	438.66 ± 10.9	97.92 ± 0.3	15.4 ± 0.8	252.4 ± 12.6
1100	469.23 ± 8.5	98.53 ± 0.2	17.9 ± 0.9	291.3 ± 14.6

they assert that the cause of inflection is a result of the dissolution of the precipitate intermetallic gamma prime phase (formed due to the presence of Ti and Al) at a specific temperature and Cr solid solution phase [57], which is equally present in the microstructure of the composites in this study. So, the inflection points experienced as the thermophysical properties increased with an increase in the heating temperature is related to the dissolution of the phases such as gamma and gamma prime and element such as Cr, Al and Ti. Besides, the contribution of GNPs is equally significant because the formation of the bilayer in GNPs initiates a further heat transfer mechanism that enables thermal transport in the sintered Ni-based composites. Correspondingly, it indicates that the formation of the bilayer in GNPs leads to a smooth phonon transition compared with few-layer and multilayer graphene [58]. It is further asserted that the smooth transition of phonon at the interface of GNPs/metal matrix might result in the increased thermal diffusivity in the sintered GNPs/IN738 composite [59]. Nevertheless, the porosity present in the composites introduced as a result of the addition of GNPs might somewhat impact the thermal diffusivity because the porosity creates space for the entrapment of gases which locally affect the behaviour of the heat transfer. Summarily, the thermophysical properties in terms of the thermal conductivity and specific heat capacity display a similar pattern with both increasing with the increasing heating temperature from RT to 600 °C. At the same time, few inflection points were observed with the thermal diffusivity of the sintered composite.

4. Discussion

The excellent improvement observed in the GNPs/IN738 composites with the increasing sintering temperature can be ascribed to the remarkable densification offered by the high sintering temperature and strengthening characteristics/properties of GNPs (superior structural integrity), diffusion/distribution of GNPs and good interfacial metallurgical bonding formed between IN738 alloy and GNPs reinforcement. Furthermore, the strengthening mechanisms that contribute to the improvement observed in the sintered composites are grain refinement ($\sigma_{Hall-Petch}$) owing to the heterogeneous nucleation of IN738 alloy on the GNPs reinforcement, beneficial load transfer from IN738 matrix to GNPs reinforcement (σ_{LT}), Orowan strengthening (σ_{orowan}) due to the hindrance of dislocation motion caused by GNPs reinforcement. The presence of GNPs promotes the formation of a pinning effect that reduces grain growth leading to the nucleation and formation

of smaller grains. The Hall–Petch effect suggests that the composites' strength increases with the formation of smaller grain sizes. Hence, the relationship could be expressed as follows in equation (1):

$$\sigma_s = \sigma_0 + kd^{-1/2} \tag{1b}$$

Where σ_0 is a constant representing either friction stress formed from dislocation glide or internal back stress, d represents the grain size of the matrix alloy, and k represents the Hall–Petch value.

It is observed that the in-situ growth and heterogeneous nucleation of IN738 matrix on the GNPs filler marginally reduce the grain size with the increasing sintering temperature in the sintered composite leading to the formation of refined grains and increase in the number of grain boundaries. Therefore, the strength of the sintered composites is improved following the Hall–Petch relation. This study observed that the average grain size of the sintered Ni-based composites at 900, 1000, 1050 and 1100 °C are 40.21, 39.34, 38.92 and 37.04 μm, respectively. Owing to the marginal decrease (nearness) in the average grain size of the sintered Ni-based composites and following Li et al. [60] report, the important contribution of the Hall–Petch strengthening mechanism (grain refinement) could be disregarded. As a result, it is not significant in this study.

The Orowan strengthening mechanism in this study is attributed to the contribution of graphene nanoplatelets reinforcement strengthening phase present within the matrix alloy of the sintered composites. It was reported in the literature by different researchers that the inclusion of nanoparticles such as GNPs as reinforcement in the matrices of metals prevents the movement of dislocations [11,61,62]. More importantly, is the fact that GNPs act as non-shearable reinforcement that helps in the pinning down of the dislocation network, which in turn promotes the bending of dislocations in the surrounding of the nanoparticle reinforcement under the effect of external force [63]. By so doing, the dislocations are accumulated within the grains and along the grain boundaries leading to an enhancement in the composite's strength. The Orowan strengthening contribution can be stated following the expression in equation (2).

$$\Delta\sigma_{Orowan} = \frac{0.13Gb}{d_r\left[\left(\frac{1}{2v_r}\right)^{1/3} - 1\right]} \cdot ln\left(\frac{d_r}{2b}\right) \tag{2}$$

Where G represents Burger's vector, b stands for the matrix shear modulus, dr represents the volume fraction of the reinforcement, and dr represents the diameter. According to Chen Z et al. [11], the nanosized graphene particles

significantly contribute to the strengthening effect of super-alloy metals. In relation to this, a 5 μm diameter and 15 nm average thickness graphene nanoplatelet reinforcement used in this study present Orowan strengthening as a critical contributor to the ultimate yield strength of the manufactured composites.

Similarly, the load transfer effect between the matrix gamma phase, graphene nanoplatelets reinforcement and precipitate gamma prime intermetallic phase under the application of an applied load promotes the complete strengthening of the manufactured Ni-based composites. The expression relating to the load-bearing strengthening of nanoparticles in metal matrices composite utilizing a modified shear lag model is shown in equation (3) [64,65].

$$\Delta\sigma_{Load\ transfer} = V_p \sigma_{um} \left[\frac{(I+t)A}{4I}\right] \tag{3}$$

Where I and t are the parallel and perpendicular size of the nanoplatelets to the direction of the force applied, σ_{um} is the yield strength of the Ni-based matrix alloy, and A represents the nanoplatelets aspect ratio, I/t. V_p is the volume fraction of the reinforcement. In the case of equiaxed particles, the expression in equation (3) is reduced thus, in equation (4) [66].

$$\Delta\sigma_{Load\ transfer} = \sigma_{um}\left(1 + AV_p\right) \tag{4}$$

The microstructure and relative density of the sintered composites at high sintering temperatures of 1050 and 1100 °C indicate the formation of minimal porosity and high densification, suggesting a strong metallurgical bonding, which may promote an effective interfacial load transfer under eternal applied force is formed [65]. Besides, Ma S. et al. [21] and Chen Z. et al. [11] concluded that the formation of good adhesion between the matrix alloy and reinforcing graphene promotes effective load transfer and improves the strength of the fabricated composites.

Apart from the contribution of graphene nanoplatelets, other phases developed are a major contributor to the overall strength of the composites. Ardell [67] argues that the precipitation strengthening of superalloys and, by extension, superalloy-based composites result from five discrete mechanisms, i.e., coherency, stacking fault, chemical composition, modulus, and order strengthening. Although not all can be present concurrently and operative simultaneously, one may have a dominant effect compared to another in a composite system [40]. Their presence and occurrence depend on different factors, such as the size of the precipitate and volume fraction [68]. Chemical strengthening is formed when there is an increase in the surface energy resulting from the formation of a new interface when a dislocation shears a precipitate. Modulus and stacking fault strengthening are developed because of the formation of different stacking fault energies and modulus of elasticity of the precipitate phase and matrix metal. There may be an occurrence of strain field around precipitates resulting from the difference in the lattice parameters of the coherent precipitate and matrix: this is known as coherency strengthening. Lastly, order strengthening could occur due to the formation of ordered crystal structure in the precipitate. This is disrupted when a dislocation penetrates through the precipitate, causing an anti-phase boundary with associated energy. These are strengthening mechanisms reported in the literature that could improve the strength of the fabricated GNPs/IN738 composites [40]. In relation to this study, there is the formation of an ordered gamma matrix phase, coherent precipitate intermetallic phase and solid solution phase, which contributes to the strengthening of the composites.

5. Conclusion

In summary, the GNPs/IN738 composite sintered at four different sintering temperatures of 900, 1000, 1050, and 1100 °C, with other parameters kept constant, were effectively manufactured by the SPS method. The study achieved the following:

- The sintering temperature positively impacts the microstructure, relative density, micro/nano hardness, tribological and thermophysical properties of the manufactured composites. The microstructure comprises the precipitate gamma, intermetallic gamma prime, and hard solid solution/GNPs phases that contribute to the strength of the composites.
- The increasing sintering temperature produces good properties with the maximum densification obtained with the sample sintered at 1100 °C. The properties are densification of 98.5%, microhardness of 469 HV, nanohardness of 17 GPa, elastic modulus of 291 GPa, wear rate of 1.149×10^{-4}, 2.636×10^{-4} and 3.142×10^{-4} mm³/Nm for 5, 10 and 20 N load and relatively good thermophysical properties with increasing temperature from 25 to 600 °C. Few points of inflection are recorded during thermophysical analysis.
- The strengthening mechanisms that contribute to the improvement in the sintered composites with the increasing sintering temperature up to 1100 °C are associated with the Hall–Petch relationship, Orowan strengthening and load transfer strengthening. Also, the phases formed as a result of using the IN738 superalloy matrix could lead to either coherency, stacking fault, chemical composition, modulus, and order strengthening behaviour, thus contributing to the improvement of the sintered composites.

Credit authorship contribution statement

Olugbenga Ogunbiyi: Conceptualization, Formal analysis, Data curation, Writing original draft. **Tamba Jamiru**: Formal analysis, writing review and editing. **Rotimi Sadiku**: Formal analysis, editing, **Salifu Smith**: Writing review, Data curation, editing. **Charity Maepa**: Data curation, Laboratory analyses.

Declaration of Competing Interest

The authors declare that they have no known competing financial interests or personal relationships that could have appeared to influence the work reported in this paper.

Acknowledgement

REFERENCES

[1] Ogunbiyi O, Jamiru T, Sadiku E, Beneke L, Adesina O, Adegbola T. Influence of sintering temperature on microstructural evolution of spark plasma sintered Inconel738LC. Procedia Manuf 2019;35:1152—7.

[2] Ogunbiyi O, Jamiru T, Sadiku E, Adesina O, Beneke L, Adegbola T. Spark plasma sintering of nickel and nickel based alloys: a Review. Procedia Manuf 2019;35:1324—9.

[3] Darolia R. Development of strong, oxidation and corrosion resistant nickel-based superalloys: critical review of challenges, progress and prospects. Int Mater Rev 2019;64(6):355—80.

[4] Haghdadi Nima, Whitelock Edward, Lim Bryan, Chen Hansheng, Liao Xiaozhou, Babu Sudarsanam S, et al. Multimodal γ′ precipitation in Inconel-738 Ni-based superalloy during electron-beam powder bed fusion additive manufacturing. J Mater Sci 2020;55(27):13342—50.

[5] Zhang X, Chen H, Xu L, Xu J, Ren X, Chen X. Cracking mechanism and susceptibility of laser melting deposited Inconel 738 superalloy. Mater Des 2019;183:108105.

[6] Engel B, Huth M, Hyde C. Numerical investigation into the influence of grain orientation distribution on the local and global elastic-plastic behaviour of polycrystalline nickel-based superalloy INC-738 LC. Crystals 2022;12(1):100.

[7] Pakseresht A, Javadi A, Bahrami M, Khodabakhshi F, Simchi A. Spark plasma sintering of a multilayer thermal barrier coating on Inconel 738 superalloy: microstructural development and hot corrosion behavior. Ceram Int 2016;42(2):2770—9.

[8] Shahwaz M, Nath P, Sen I. A critical review on the microstructure and mechanical properties correlation of additively manufactured nickel-based superalloys. J Alloys Compd 2022:164530.

[9] Rani S, Agrawal AK, Rastogi V. Failure analysis of a first stage IN738 gas turbine blade tip cracking in a thermal power plant. Case studies in engineering failure analysis 2017;8:1—10.

[10] Chen Yuan, Lu Fenggui, Zhang Ke, Nie Pulin, Hosseini Seyed Reza Elmi, Feng Kai, et al. Laser powder deposition of carbon nanotube reinforced nickel-based superalloy Inconel 718. Carbon 2016;107:361—70.

[11] Chen Zhen, Zhang Shuzhe, Lu Bingheng, Zhang Lijuan, Yang Xigang, et al. Graphene reinforced nickel-based superalloy composites fabricated by additive manufacturing. Mater Sci Eng, A 2020;769:138484.

[12] Yu W, Sisi L, Haiyan Y, Jie L. Progress in the functional modification of graphene/graphene oxide: a review. RSC Adv 2020;10(26):15328—45.

[13] Han B, Li G, Chen Z, Zhang G. Microstructure and wear property of graphene nanoplatelets reinforced nickel-based composite coating by laser cladding. Metals 2022;12(8):1247.

[14] Yi D, Li X, Wang C, Zhang J, Yang X, Zhang D. Formation and influence of graphene in Inconel 625 prepared by selective laser melting. J Alloys Compd 2021;878:160310.

[15] Gao Y, Zou J, Wang X, Wang X, Yang J, Wang H. Microstructure and mechanical performance of graphene nanosheets reinforced Nickel-based superalloy FGH95 composite. Nanomaterials 2020;10(1):100.

[16] Ogunbiyi O, Jamiru T, Sadiku E, Adesina O, Salifu S, Beneke L. Effect of nickel powder particle size on the microstructure and thermophysical properties of spark plasma sintered NiCrCoAlTiW-Ta superalloy. In: IOP conference series: materials science and engineering. vol. 655. IOP Publishing; 2019, 012031. 1.

[17] Ogunbiyi O, Sadiku E, Jamiru T, Adesina O, Beneke L. Spark plasma sintering of Inconel 738LC: densification and microstructural characteristics. Mater Res Express 2019;6(10):1065g8.

[18] Jeje SO, Shongwe MB, Rominiyi AL, Olubambi PA. Spark plasma sintering of titanium matrix composite—a review. Int J Adv Manuf Technol 2021;117(9):2529—44.

[19] Makena IM, Shongwe MB, Ramakokovhu MM, Lethabane ML. A review on sintered nickel based alloys. Proceedings of the World Congress on Engineering 2017;2:922—7.

[20] Meng B, Zhang Z, Ma L, Wan M. Effect of sintering temperature on microstructure and mechanical properties of Inconel 718 superalloy prepared by micro-FAST. Mater Sci Eng, A 2022;836:142733.

[21] Ma Shuan, Yang Yanjie, Li Ang, Zhou Shiqi, Shi Lan, Wang Shaolan, et al. Effects of temperature on microstructure and mechanical properties of IN718 reinforced by reduced graphene oxide through spark plasma sintering. J Alloys Compd 2018;767:675—81.

[22] Rominiyi AL, Shongwe MB, Maledi N, Babalola BJ, Olubambi PA. Synthesis, microstructural and phase evolution in Ti—2Ni and Ti—10Ni binary alloys consolidated by spark plasma sintering technique. Int J Adv Manuf Technol 2019;104(1):1041—9.

[23] Bayode B, Teffo M, Tayler T, Ige O, Machaka R, Olubambi P. Structural, mechanical and electrochemical properties of spark plasma sintered Ti-30Ta alloys. Mater Sci Eng, B 2022;283:115826.

[24] Jeje Samson Olaitan, Shongwe Mxolisi Brendon, Maledi Nthabiseng, Ogunmuyiwa Enoch Nifise, Tshabalala Lerato Criselda, Babalola Bukola Joseph, et al. Sintering behavior and alloying elements effects on the properties of CP-Titanium sintered using pulsed electric current. Mater Chem Phys 2020;256:123707.

[25] Ogunbiyi O, Jamiru T, Sadiku R, Beneke L, Adesina O, Fayomi J. Influence of sintering temperature on the corrosion and wear behaviour of spark plasma—sintered Inconel 738LC alloy. Int J Adv Manuf Technol 2019;104(9—12):4195—206.

[26] Xu Z, Jia C, Kuang C, Chu K, Qu X. Spark plasma sintering of nitrogen-containing nickel-free stainless steel powders and effect of sintering temperature. J Alloys Compd 2009;484(1—2):924—8.

[27] Yamanoglu R, Bradbury W, Karakulak E, Olevsky E, German R. Characterisation of nickel alloy powders processed by spark plasma sintering. Powder Metall 2014;57(5):380—6.

[28] Ujah CO, Popoola PA, Popoola O, Uyor UO. Mechanical and thermal behaviors of Ti36-Al16-V16-Fe16-Cr16 high entropy alloys fabricated by spark plasma sintering: an advanced material for high temperature/strength applications. J Compos Mater 2022;56(26):3913—23.

[29] Okoro AM, Machaka R, Lephuthing SS, Oke SR, Awotunde MA, Olubambi PA. Nanoindentation studies of the

mechanical behaviours of spark plasma sintered multiwall carbon nanotubes reinforced Ti6Al4V nanocomposites. Mater Sci Eng, A 2019;765:138320.

[30] Dada M, Popoola P, Mathe N, Adeosun S, Pityana S. Investigating the elastic modulus and hardness properties of a high entropy alloy coating using nanoindentation. International Journal of Lightweight Materials and Manufacture 2021;4(3):339–45.

[31] Wall M. The Raman spectroscopy of graphene and the determination of layer thickness. Therm Sci 2011;5:1–5.

[32] Ogunbiyi O, Jamiru T, Sadiku E, Beneke L, Adesina O, Adegbola T. Microstructural characteristics and thermophysical properties of spark plasma sintered Inconel 738LC. Int J Adv Manuf Technol 2019;104(1–4):1425–36.

[33] Mignanelli PM, Jones NG, Pickering EJ, Messé OMDM, Rae CMF, Hardy MC, et al. Gamma-gamma prime-gamma double prime dual-superlattice superalloys. Scripta Mater 2017;136:136–40.

[34] Ogunbiyi O, Sadiku R, Adesina O, Adesina OS, Salifu S, Fayomi J. Microstructure and mechanical properties of spark plasma-sintered graphene-reinforced Inconel 738 low carbon superalloy. Metall Mater Trans 2021:1–15.

[35] Zhang Xiaoyu, Zhang Jingfan, Chen Xin, Wu Yanxia, et al. In-situ grown few-layer graphene reinforced Ni matrix composites with simultaneously enhanced strength and ductility. Mater Sci Eng, A 2021;828:142118.

[36] Wang Y, Shi J, Lu S, Wang Y. Selective laser melting of graphene-reinforced Inconel 718 superalloy: evaluation of microstructure and tensile performance. J Manuf Sci Eng 2017;139(4):041005.

[37] Lei Y, Jiang J, Bi T, Du J, Pang X. Tribological behavior of in situ fabricated graphene–nickel matrix composites. RSC Adv 2018;8(39):22113–21.

[38] Hakeem Abbas Saeed, Patel Faheemuddin, Minhas Naeem, Malkawi Ameen, Aleid Zahra, Ehsan Muhammad Ali, et al. Comparative evaluation of thermal and mechanical properties of nickel alloy 718 prepared using selective laser melting, spark plasma sintering, and casting methods. J Mater Res Technol 2021;12:870–81.

[39] Borkar Tushar, Mohseni Hamidreza, Hwang Junyeon, Scharf Thomas W, Tiley Jaimie S, Hong Soon H, et al. Excellent strength–ductility combination in nickel-graphite nanoplatelet (GNP/Ni) nanocomposites. J Alloys Compd 2015;646:135–44.

[40] Goodfellow A. Strengthening mechanisms in polycrystalline nickel-based superalloys. Mater Sci Technol 2018;34(15):1793–808.

[41] Xiao W-h, Lu S-q, Wang Y-c, Jing S. Mechanical and tribological behaviors of graphene/Inconel 718 composites. Trans Nonferrous Metals Soc China 2018;28(10):1958–69.

[42] Xu J, Yi D-Q, Cui Q, Wang B. Enhanced wear resistance of Ni/h-BN composites with graphene addition produced by spark plasma sintering. Acta Metall Sin 2019;32(7):876–86.

[43] Thomas S, Thomas R, Zachariah AK, Mishra RK. Spectroscopic methods for nanomaterials characterization. Elsevier; 2017.

[44] Chong L, Guo H, Zhang Y, Hu Y, Zhang Y. Raman study of strain relaxation from grain boundaries in epitaxial graphene grown by chemical vapor deposition on SiC. Nanomaterials 2019;9(3):372.

[45] Shahin M, Munir K, Wen C, Li Y. Magnesium-based composites reinforced with graphene nanoplatelets as biodegradable implant materials. J Alloys Compd 2020;828:154461.

[46] Oketola A, Jamiru T, Adegbola AT, Ogunbiyi O, Sadiku R, Salifu S. Influence of sintering temperature on the microstructure, mechanical and tribological properties of ZrO2 reinforced spark plasma sintered Ni–Cr. International

Journal of Lightweight Materials and Manufacture 2022;5(2):188–96.

[47] Rominiyi AL, Shongwe MB, Jeje SO, Olubambi PA. Microstructure, tribological and oxidation behaviour of spark plasma sintered Ti-Ni-xTiCN composites. J Alloys Compd 2022;890:161857.

[48] Rominiyi AL, Shongwe MB, Ogunmuyiwa EN, Babalola BJ, Lepele PF, Olubambi PA. Effect of nickel addition on densification, microstructure and wear behaviour of spark plasma sintered CP-titanium. Mater Chem Phys 2020;240:122130.

[49] Belmonte M, Ramírez C, González-Julián J, Schneider J, Miranzo P, Osendi MI. The beneficial effect of graphene nanofillers on the tribological performance of ceramics. Carbon 2013;61:431–5.

[50] Ogunbiyi O, Jamiru T, Sadiku R, Adesina O, Adesina OS, Obadele BA. Spark plasma sintering of graphene-reinforced Inconel 738LC alloy: wear and corrosion performance. Met Mater Int 2020:1–15.

[51] Xu Z, Shi X, Zhai W, Yao J, Song S, Zhang Q. Preparation and tribological properties of TiAl matrix composites reinforced by multilayer graphene. Carbon 2014;67:168–77.

[52] Falodun Oluwasegun Eso, Obadele Babatunde Abiodun, Oke Samuel Ranti, Ige Oladeji Oluremi, Olubambi Peter Apata, Lethabane Moipone Linda, et al. Influence of spark plasma sintering on microstructure and wear behaviour of Ti-6Al-4V reinforced with nanosized TiN. Trans Nonferrous Metals Soc China 2018;28(1):47–54.

[53] Zhai Wenzheng, Shi Xiaoliang, Wang Mang, Xu Zengshi, Yao Jie, Song Siyuan, et al. Grain refinement: a mechanism for graphene nanoplatelets to reduce friction and wear of Ni3Al matrix self-lubricating composites. Wear 2014;310(1–2):33–40.

[54] Tiwari Jitendar Kumar, Mandal Ajay, Sathish N, Kumar Surender, Ashiq Mohammed, Nagini M, et al. Effect of graphene addition on thermal behavior of 3D printed graphene/AlSi10Mg composite. J Alloys Compd 2022;890:161725.

[55] Yang L, Chang K-M, Mannan S, deBarbadillo J. A new DTA approach for verifying precipitate solvus in Inconel alloy 718. Superalloys 1997;718:353–65. 625, 706 and various derivatives.

[56] Rai AK, Trpathy H, Hajra R, Raju S, Saroja S. Thermophysical properties of Ni based super alloy 617. J Alloys Compd 2017;698:442–50.

[57] Yang L, Chang K-M, Mannan S, deBarbadillo J. A new DTA approach for verifying precipitate solvus in Inconel Alloy 718(Differential Thermal Analysis). Superalloys 1997;718:353–65. 625, 706 and various derivatives.

[58] Boden A, Boerner B, Kusch P, Firkowska I, Reich S. Nanoplatelet size to control the alignment and thermal conductivity in copper–graphite composites. Nano Lett 2014;14(6):3640–4.

[59] Jagannadham K. Orientation dependence of thermal conductivity in copper-graphene composites. J Appl Phys 2011;110(7):074901.

[60] Li P, Yang H, Gao M. Microstructure and mechanical properties of multi-scale in-situ Mg2Si and CNTs hybrid reinforced AZ91D composites. J Mater Res Technol 2021;14:2471–85.

[61] Hu Zengrong, Tong Guoquan, Dong Lin, Nian Qiong, Shao Jiayi, Hu Yaowu, et al. Laser sintered graphene nickel nanocomposites. J Mater Process Technol 2016;231:143–50.

[62] Güler Ö, Bağci N. A short review on mechanical properties of graphene reinforced metal matrix composites. J Mater Res Technol 2020;9(3):6808–33.

[63] Patil A, Nartu MSKKY, Ozdemir F, Banerjee R, Gupta RK, Borkar T. Enhancement of the mechanical properties of

graphene nanoplatelet (GNP) reinforced nickel matrix nanocomposites. Mater Sci Eng, A 2021;817:141324.

[64] Jeje SO, Shongwe MB, Maledi N, Rominiyi AL, Adesina OS, Olubambi PA. Synthesis and characterization of TiN nanoceramic reinforced Ti−7Al−1Mo composite produced by spark plasma sintering. Mater Sci Eng, A 2021;807:140904.

[65] Gao Yuxi, Zou Jinwen, Wang Xiaofeng, Yang Jie, Li Zhuo, Li Jia, et al. Mechanical properties of powder metallurgy nickel-based superalloy composite reinforced by low content graphene nanosheets. Adv Eng Mater 2020;22(7):2000156.

[66] Tang Y, Yang X, Wang R, Li M. Enhancement of the mechanical properties of graphene−copper composites with graphene−nickel hybrids. Mater Sci Eng, A 2014;599:247−54.

[67] Ardell AJ. Precipitation hardening. Metall Trans A 1985;16(12):2131−65.

[68] Ahmadi M, Povoden-Karadeniz E, Whitmore L, Stockinger M, Falahati A, Kozeschnik E. Yield strength prediction in Ni-base alloy 718Plus based on thermo-kinetic precipitation simulation. Mater Sci Eng, A 2014;608:114−22.